# A simulation-driven spectrometric method to determine $\alpha$ particle attenuation in air filters

Luca Terray, Pierre-Jean Gauthier, Vincent Breton

# A simulation-driven spectrometric method to determine $\alpha$ particle attenuation in air filters

Luca Terray[a,b,*], Pierre-Jean Gauthier[a], Vincent Breton[b]

[a] *Université Clermont Auvergne, Laboratoire Magmas et Volcans, 6 avenue Blaise Pascal, 63170 Aubière, France*
[b] *Université Clermont Auvergne, Laboratoire de Physique de Clermont, 4 avenue Blaise Pascal, 63170 Aubière, France*

**Abstract**

The analysis of $\alpha$ radioactivity in air is often performed on filters in order to collect large amounts of radionuclides on a small surface and therefore, increase the measurement sensitivity. The same approach has been used for decades in the field of volcanology, where $^{210}$Po activities are commonly analyzed in volcanic aerosols collected on filters in order to better understand magma processes at depth. However, the attenuation of $\alpha$ particles interacting with the filter matrix generally lowers the detection efficiency, which needs to be corrected in order to obtain accurate activities. In this contribution, we present a correction method performing a decomposition of the energy spectrum recorded by the detector over a base of simulated spectra corresponding to different depths of $\alpha$ particle emission. These simulations are obtained by using the GATE code in order to describe both the detector environment and $\alpha$ particles trajectories and interactions. The method based on the retrieval of the information conveyed by the spectra uses a regular linear inversion process. We validated this approach using natural radioactive aerosols of radon daughters ($^{214}$Po) filtered on two different types of media (PTFE and cellulose acetate) and we found a good agreement between the activity corrected for attenuation using the $\alpha$ spectrum and the total activity determined from simultaneous $\gamma$ spectrometry of $^{214}$Bi, in radioactive equilibrium with its very short half-life daugther $^{214}$Po.

*Corresponding author: terray@phare.normalesup.org

*Keywords:* $\alpha$ attenuation, filters, $\alpha$ spectrometry, radon daughters, inversion

## 1. Introduction

The radioactivity of aerosol particles from both atmospheric and indoor air as well as other terrestrial fluids like volcanic gases is often measured on filters where airborne particulate matter can be easily accumulated. This approach allows very high sensitivity thanks to the concentration on a small surface of the whole particulate matter content of large volumes of air. Filters are hence widely used for air monitoring or low radioactivity environmental studies. In most cases, $\alpha$ radioactivity is direclty measured on the filter using an $\alpha$ counter or spectrometer. While this method is convenient because it does not require any sample preparation, it also has an important drawback known as $\alpha$ self-absorption or $\alpha$ attenuation [e.g. 1]. It has been indeed shown that $\alpha$ particles emitted by filtrated radioactive aerosols can partly or even totally lose their energy by interaction with filter fibers [2], other nuclide-carrying aerosol particles [3] and filtrated particulate matter [2, 4]. This ultimately prevents their detection and modify the overall efficiency of the measurement. Attenuation of $\alpha$ particles in filters can consequently be responsible for an underestimation of the actual activity by several tens of percent [5, 6].

For the needs of radioactivity monitoring, $\alpha$ attenuation in air filters has been extensively studied in relation with various experimental parameters such as filter type [2], filtration velocity [1, 7], aerosol particle size and shape [3], or dust loading [6]. Correction factors and tables have been proposed by comparing the total and the attenuated $\alpha$ activities on a large set of filters covering different filter types, filtration velocities, and dust loading [e.g., 1, 5, 6]. However, due to the diversity in filters and sampling conditions, such studies unfortunately can not cover all possible configurations.

In order to address this issue, numerical approaches have been developed by several groups [8, 9]. They rely on Monte-Carlo simulation of $\alpha$ particles interaction with matter to compute both the $\alpha$ energy spectrum and the at-

tenuation factor for any filtration configuration. Different softwares have been used for this purpose, including dedicated tools [8] or broader-scope codes like MCNPX [9]. Thanks to the versatility of these numerical frameworks, any measurement geometry and any filter composition and density (possibly including sampled particulate matter) can be treated making the numerical approach very attractive. Its only but serious counterpart regards the need of accurately constraining the various parameters involved in running a simulation. While both filter density and composition are generally well known and constant, the depth distribution of aerosol particles inside the filter is much more variable and complex to assess. Yet, $\alpha$ particle depth-of-emission strongly controls its attenuation within the filter. Consequently, the numerical approach requires an estimation of the burial depth of $\alpha$ emitters within the filter. Such an estimate can be for instance obtained from peeling measurement [9] or numerical simulation of the filtration process [10]. However, these solutions are too time-consuming to be fully adapted for the treatment of a large number of filters with variable $\alpha$ attenuation. Alternatively, the depth profile can be estimated with a simple trial-and-error method, comparing the experimental and simulated energy spectra until a good match is found [11]. The main drawback of this latter strategy is the need of a prior knowledge of the depth-distribution and some kind of intelligence (either human or artificial) in order to converge.

In this article we present a new method to infer a likely depth-distribution of aerosol particles from the shape of the $\alpha$ energy spectrum. This method needs no prior knowledge about the depth-distribution and is not based on any random exploration of the solution space, making it much more straightforward and robust than the trial-and-error method of [11]. This method relies on the decomposition of the measured $\alpha$ energy spectrum with a combination of simulated spectra corresponding to different depths of $\alpha$ emission within the filter. It is then possible to determine the overall $\alpha$ attenuation coefficient for the whole filter from the inferred depth-distribution. The method presented here has been developed using filter samples taken in a radon-rich natural environment. The presence of large amounts of radon daughters (namely $^{218}$Po, $^{214}$Pb, $^{214}$Bi and

$^{214}$Po in their successive order of decay) on filter samples allowed precise determination of both $^{214}$Po $\alpha$ emissions and $^{214}$Bi $\gamma$ emissions. These results were used to assess the validity of our approach in determining $\alpha$ attenuation in atmospheric filters but the proposed methodology could apply to any natural or artificial $\alpha$-emitter trapped in a filter.

## 2. Experimental setup

The following experiment was designed by our group while working on radionuclide emissions from active volcanoes [12, 13]. The experimental setup used in this study thus directly derives from key constraints encountered in the field. These include the need for rather short sampling durations, the selection of given filtration media, as well as the use of a light, portable nuclear spectrometer. Details on the experimental setup are given in the following sub-sections.

### *2.1. Radioactive aerosol sampling by filtration*

The study was performed in a radon-rich underground cellar located in the historical center of Clermont-Ferrand (France). Radon activity in the air was measured during the experiment with an electronic dosimeter (Radon Eye PLUS2 from the FTLAB Company, S. Korea) at ca. $1200\,\mathrm{Bq\,m^{-3}}$. At such radon activity levels, large amounts of short-lived radon daughters are readily available in the air as radioactive aerosols. The aerosol fraction, which can be sampled by filtration, is indeed naturally produced by the adsorption of airborne $^{222}$Rn daughters on pre-existing aerosol particles or even by nucleation of aerosol particles on free daughter atoms. Such a radon-rich environment thus gives easy access to a natural source of radioactive aerosol, hence making an alternative solution for laboratories that are not equipped with an aeorosol generation facility [e.g. 14].

We used two different types of filters. The first one is made of cellulose acetate fibers (Poelmann-Schneider, blue type, from the CAMFIL Company, France, referred to as CA in the following). It was chosen because it has long

been employed to characterize the radioactivity of volcanic plumes [12, 15, 16]. Cellulose acetate filters are also frequently used for the purpose of air monitoring [e.g. 14]. The second one is a polytetrafluoroethylene membrane filter from the Sterlitech Company, USA (referred to as PTFE in the following). PTFE membranes are not suited for high-volume air samplers due to their rapid clogging and significant pressure drops but are rather used in low-volume applications requiring a high filtration efficiency. Such PTFE membranes are therefore increasingly used for scientific applications like volcanology [17]. Table 1 gives the characteristics of both types of filters in terms of geometry (thickness, diameter), chemical composition, apparent density and bulk porosity. For each filter type, the chemical formula of cellulose acetate ($C_2H_4O_2$) and PTFE ($C_2F_4$) were merely used. Apparent density was obtained by measuring the volume and the mass of each filter and porosity was then calculated by comparing apparent density with the density of pure cellulose acetate and polytetrafluoroethylene.

At radon levels higher than $1000\,\mathrm{Bq\,m^{-3}}$, large amounts of daughter products (up to thousands of Bq) can be accumulated on filters, even for short sampling durations using a vacuum pump providing a moderate flowrate between a few $\mathrm{m^3\,h^{-1}}$ to tens of $\mathrm{m^3\,h^{-1}}$. Sampling specifications (flowrate, duration) are detailed in Table 1. Such high radon levels are common in poorly-ventilated buildings [e.g., 18] which makes the methodology presented in this paper easily reproducible, as it would be for other $\alpha$-emitters provided that a dedicated numerical treatment is applied (see section 4.1).

### *2.2. Measurement methodology and analytical setup*

Among the four short-lived $^{222}$Rn daughters, both $^{218}$Po and $^{214}$Po are $\alpha$ emitters and, in theory, both can be used to study $\alpha$ attenuation in air filters. However, because $^{218}$Po - the first $^{222}$Rn daughter - is not supported by radioactive decay on the filter which cannot retain gaseous radon, any attempt to measure its activity must be made within at most 15 minutes after sampling. While a filter can be measured by $\alpha$ counting or $\alpha$ spectrometry right after sampling in order to derive $^{218}$Po apparent activity (i.e., underestimated because of $\alpha$ attenuation), determination of actual $^{218}$Po activity requires radiochem-

Table 1: Characteristics of filters used in this study and sampling information (flowrate, duration). The uncertainties on apparent density and bulk porosity only derive from the uncertainty on the filter thickness (all uncertainties are given at $2\sigma$).

| Filter code $\alpha$ | CA | PTFE |
|---|---|---|
| Type | Fibrous filter | Membrane filter |
| Provider | CAMFIL | Sterlitech |
| Pore size | unknown | 1 µm |
| Diameter | 90 mm | 82 mm |
| Thickness | 225(10) µm | 90(10) µm |
| Mass | 513 mg | 183 mg |
| Chemical formula | $C_2H_4O_2$ | $C_2F_4$ |
| Pure density | $1.3\,\mathrm{g\,cm^{-3}}$ | $2.2\,\mathrm{g\,cm^{-3}}$ |
| Apparent density | $0.358(16)\,\mathrm{g\,cm^{-3}}$ | $0.390(43)\,\mathrm{g\,cm^{-3}}$ |
| Bulk porosity | 72.5(12) % | 82.3(19) % |
| Flowrate | $23\,\mathrm{m^3\,h^{-1}}$ | $8.5\,\mathrm{m^3\,h^{-1}}$ |
| Sampling duration | 30 min | 30 min |

ical separation and $\alpha$ spectrometry. This cannot be achieved in such a short timelapse, making the use of $^{218}$Po unsuitable for the direct determination of $\alpha$ attenuation.

Contrastingly, the shortest-lived $^{214}$Po (half-life of 164 µs) reaches radioactive equilibrium with $^{214}$Bi in a few ms. Due to the relatively long half-life of $^{214}$Bi (19.8 minutes) and to $^{214}$Bi regeneration by $^{214}$Pb decay (half-life of 27 minutes), both $^{214}$Po apparent and actual activities remain measurable for two to three hours after sampling. Therefore, determination of $^{214}$Po attenuation using radiochemical techniques could be envisaged in favorable conditions but mostly remains difficult to achieve, especially when filters are taken in remote locations. Nevertheless, the whole $^{214}$Po activity in the filter can be indirectly determined by measuring the activity of $^{214}$Bi with a $\gamma$ spectrometer. This indirect measurement relies on the radioactive equilibrium between $^{214}$Bi and $^{214}$Po activities and on the negligible attenuation of $^{214}$Bi 609 keV $\gamma$ rays by the filter.

To achieve these measurements, we developed a portable nuclear spectrometer powered by Li batteries, which can be easily transported in a portable field case ($45 \times 26 \times 15$ cm). Technical details on this device as well as its specifications will be published elsewhere. Nevertheless, we mention here that we used a silicium detector of 46.5 mm active diameter (Canberra CAM PIPS 1700) polarized at 24 V and connected at its specific preamplifier (Canberra 2003T) in order to retrieve the $\alpha$ spectrum of the filters. The filter was positioned with a mechanical holder parallel to the Si detector and at a distance of 1.8(2) mm (the space between the filter and the detector surface is occupied by air). At the rear of the filter, we placed a sodium iodide scintillator (NaI (Tl)) coupled with a photo-multiplier tube (Canberra NaI 802 2x2) and connected to a preamplifier (Canberra 2007P) for simultaneous $\gamma$ spectrum measurements. The outputs of both detectors were read by a digital spectroscopy system (CAEN DT524) connected to a computer.

In order to analyze $^{214}$Po in filter samples in a low-radon environment, the spectrometer was operated outside of the cellar, at street level. The instrumental background was monitored prior to any sample acquisition and was found

negligible for the $\alpha$ detector. This is not the case for the $\gamma$ background which records the contribution of cosmic rays and terrestrial $\gamma$ emitters, among which radon daughters present in the air. However, for the area of the $^{214}$Bi peak at 609 keV, background was found as low as 1 % of the total peak area recorded for samples. Finally, the presence of the shortest-lived $^{218}$Po collected along with $^{214}$Po on filters is likely to interfer the recorded $\alpha$ spectrum since both isotopes have close decay energies. In order to get rid of $^{218}$Po in the filter, we started the filter measurement 18 min after sampling (i.e., 6 periods of $^{218}$Po) in order to have a $\approx$ 60-fold reduction of its initial activity (see time delays between end of sampling and start of counting, given in Table 2).

## 3. Experimental results

Experimental $\alpha$ spectra obtained for each filter type (CA and PTFE) are represented in Figure 1. The contribution of $^{212}$Po (a progeny of $^{220}$Rn in equilibrium with its parent $^{212}$Pb) to the $^{214}$Po peak was found to be lower than 0.1% in both cases and was neglected.

The two spectra were normalized (see figure caption) in order to be comparable in terms of shape. It clearly appears that, even if the two spectra peak at the same energy (7400 keV), their shape is very different. The PTFE spectrum is much sharper than the CA spectrum which presents a prominent low-energy tail. This feature can be interpreted as a much more important $\alpha$ attenuation for CA with respect to PTFE membranes. Along with the $\alpha$ spectrum, the $\gamma$ spectrum was simultaneously acquired with the NaI(Tl) scintillator, allowing direct determination of $^{214}$Bi through its 609 keV ray (Figure 2). Both $^{214}$Po counting rate ($\alpha$) and $^{214}$Bi activity ($\gamma$) measured for each filter are reported in Table 2. From these two values, $\alpha$ detection efficiency can be derived since radioactive equilibrium is always maintained within the pair $^{214}$Bi-$^{214}$Po. It can been readily seen that the overall efficiency for CA is significantly smaller compared to the PTFE filter, with an efficiency difference of nearly 10 %.

Based on the observation of flattened $\alpha$ spectrum associated to lower $\alpha$ detection efficiency, both likely reflecting enhanced $\alpha$ energy absorption within

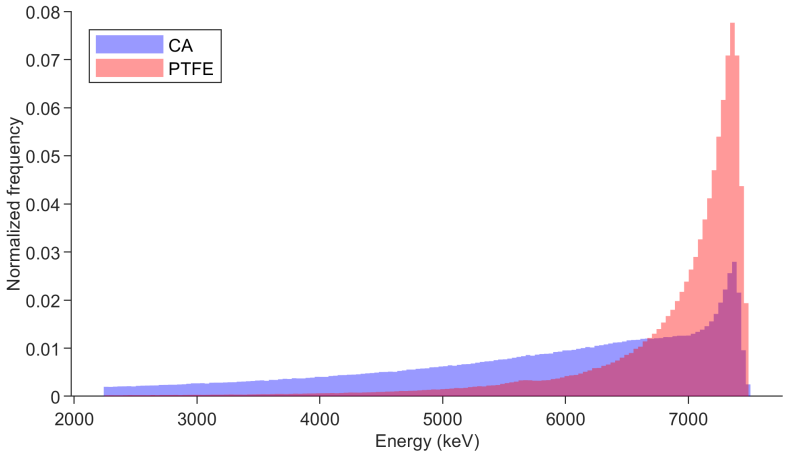


Figure 1: Comparison of $^{214}$Po spectra measured on CA and PTFE filters. The two spectra have been normalized to the total number of counts. The peak position ($\approx$ 7400 keV) is significantly below the $\alpha$ particle initial energy for $^{214}$Po (7833 keV), because of attenuation in the air layer between the filter and the detector. The good agreement in peak positions for the two filters suggests that the counting geometry is well preserved between two consecutive measurements.

Table 2: Parameters (duration, time delay between sampling end and counting) and results of nuclear measurements of CA and PTFE filters. $^{214}$Po counting rate is taken in the energy window from 2250 keV to 7500 keV. Uncertainties are given at $2\sigma$ and mostly originate from counting statistics and fit uncertainties. The filters were not collected in the same time, therefore it is not possible to compare the two filters in terms of filtration efficiency. cpm stands for count per minute, and dpm for disintegration per minute (1 dpm = 1/60 Bq).

| Filter code $\alpha$ | CA | PTFE |
|---|---|---|
| Delay before counting | 17m15s | 17m30s |
| Counting duration | 01h04m32s | 01h02m15s |
| $^{214}$Po counting rate | $42.93(6) \times 10^3$ cpm | $24.39(4) \times 10^3$ cpm |
| $^{214}$Bi activity | $132(1) \times 10^3$ dpm | $61.4(9) \times 10^3$ dpm |
| $^{214}$Po detection efficiency | 32.6(3) % | 39.8(6) % |

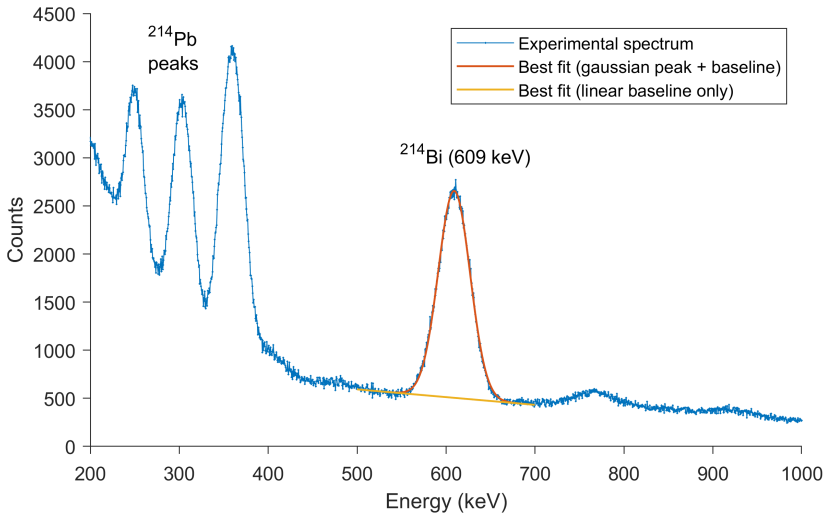


Figure 2: $\gamma$ energy spectrum measured for PTFE membrane in the region 200 keV to 1000 keV. The 609 keV peak of $^{214}$Bi is clearly present as well as the three peaks of $^{214}$Pb (242 keV, 295 keV and 352 keV). $^{214}$Bi activity in the filter was determined by fitting the 609 keV peak with a gaussian curve on a linear baseline.

CA filters, we developed a numerical approach based on Monte Carlo simulations in order to reproduce experimental spectra and determine $\alpha$ attenuation.

## 4. Numerical simulation

### *4.1. Framework of Monte Carlo simulations*

$\alpha$ attenuation in the filter was simulated using the GATE code [19]. GATE is an opensource code designed for Monte-Carlo simulations in medical imaging and radiotherapy. It is based on GEANT4 code developped at CERN for the simulation of particle interaction with matter [20]. A GATE simulation requires the definition of a geometry (including material characteristics), a source (type, energy and position), a physics set (list of physical interactions simulated), and an actor (indicating the information to be retrieved). Following the work of [9], we did not try to reproduce the intertwining of fibers but rather defined

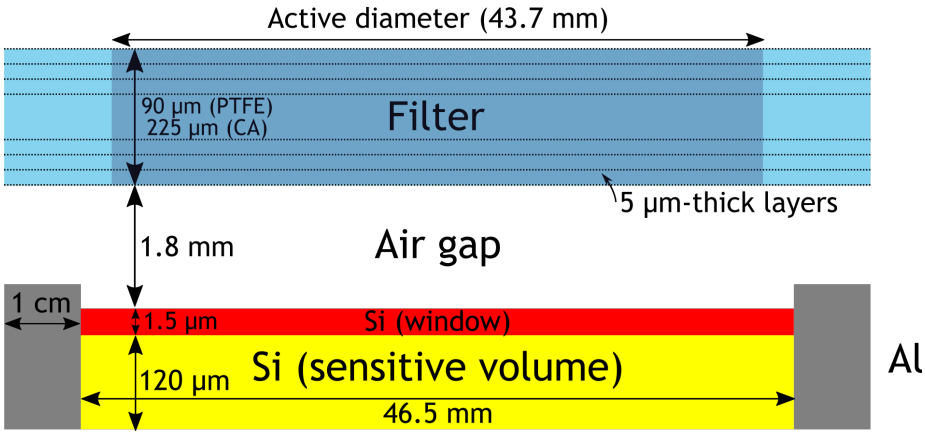


Figure 3: Representation of the $\alpha$ Si detector and the filter in GATE.

the geometry of the filter as an homogeneous cylinder filled with cellulose acetate or PTFE, using apparent densities and compositions indicated in Table 1. Moreover, we assumed the $\alpha$ attenuation due to aerosol particles is negligible compared to the attenuation occuring by interaction with the filter itself. This assumption is justified by the low mass of collected aerosol particles: considering a likely concentration of aerosol particles of $10\,\mu g\,m^{-3}$ [21, 22] and $10\,m^3$ of sampled air, we obtain a particulate mass of 100 µg, that is to say less than 0.1 % of the total mass of the filter. However, in conditions of high dust loading this assumption should be obviously revised.

The detector geometry was defined as two adjacent cylinders of 46.5 mm diameter. The first cylinder (see Figure 3) corresponds to the protection layer of the detector. According to the constructor, this window is responsible for an $\alpha$ attenuation equivalent to 1.5 µm of Si. Because its real composition and thickness are unknown, its thickness was set to 1.5 µm and it was filled with pure Si, so as to reproduce the $\alpha$ energy attenuation specified by the constructor. The second cylinder corresponds to the sensitive volume of the detector. Based on detector specifications, it has a 100 µm thickness for 24V polarization. The detector was positioned parallel to the filter surface at a distance of 1.8 mm. The detection environment was filled with air at the density corresponding with

local P-T conditions ($1150\,\mathrm{g\,m^{-3}}$). The source was set to emit $\alpha$ particles of 7833.46 keV ($^{214}$Po) isotropically (note that energy could be set at any other appropriate value for studying the $\alpha$ absorption of other $\alpha$ emitters). In Geant4 environment, an emission of primary particle (here an $\alpha$ particle) is called an event. Even if aerosol particles deposition is likely to decrease along the radial axis due to flow rate diminution toward the rim of the filter, this effect has been shown to be lower than 10 % for coarse mode particles and 4 % for fine mode particles [e.g., 23, for a comparable flow rate to filter surface ratio]. We thus assumed that the deposition of radioactive aerosols is horizontally homogeneous (no radial variation and no azimuthal variation due to cylindrical symmetry). Therefore, for each event in the simulation, the horizontal position of $\alpha$ emission was randomly chosen following uniform radial and azimuthal distributions. In order to assess the effect of $\alpha$ emission depth on $\alpha$ attenuation, different depths were defined in the simulation. The filter was defined as a succession of 5 µm-thick layers (see Figure 3), which approximately corresponds to the geometrical diameters of both CA fibers and bigger aerosol particles. A vertical resolution better than 5 µm would thus yield unsupported precision, because most of the density heterogeneity is expected to occur at a micrometric spatial scale (due to the porosity and aerosol particles). For each 5 µm layer within the filter (i.e., from below the exposed surface down to the rear of the filter), a simulation was performed considering the whole amount of $\alpha$ emitters to be contained within this given layer. Such a step discretization approach of the aerosol depth-distribution within the whole filter was run for each individual layer by assuming a homogeneous distribution of aerosols contained in it. Another run was finally performed considering $\alpha$ emission entirely originates from the surface of the filter. In total, 19 and 46 runs were processed for each filter (CA and PTFE, respectively), i.e. 65 runs in total. The physics package was set to be *emstandard option 3*, which is a GEANT4 package adapted to electron and hadron tracking in matter. An energy actor was defined to retrieve the total energy deposited in the sensitive volume of the Si detector for each $\alpha$ emission event. For each run, 100 000 $\alpha$ particles were launched and tracked. At the end

of each run, the actor generated an energy histogram corresponding to the $\alpha$ energy deposited in the detector per event. The resolution of the detector was taken into account in offline mode, by convolution of the simulated $\alpha$ spectrum with a fixed 90 keV gaussian noise using the Box-Mueller algorithm described in [24].

The simulation procedure was validated using a $^{238}$Pu reference source. The measured efficiency was determined at 41.7(14) % ($2\sigma$) by counting the source with the silicium detector. The detection efficiency simulated with GATE was in good agreement with this value, averaging 41.3(1) % ($2\sigma$). The 1 % relative difference between the two approaches (i.e. 0.4/41.3) is smaller than the $2\sigma$relative uncertainty on the source reference activity (3.4 %), which can then be considered as the confidence interval length to apply to the simulated efficiencies.

### *4.2. Results of GATE simulations*

For both filter types, the detection efficiency (Figure 4) and energy spectrum (Figure 5) obtained from GATE simulations are drawn as a function of $\alpha$-emission depth. The $^{214}$Po detection efficiency clearly decreases with the depth of emission inside the filter, starting from 41 % at the surface for both filters and droping down to 26 % for PTFE and 0 % for CA at the bottom of the filter. Both filters show a very similar decreasing pattern, as expected since the mass and electronic densities of the two materials are very close (see Table 1). Nevertheless, detection efficiency for CA filters decreases faster, which can be interpreted as the result of a slighlty higher $Z/A$ ratio for CA material compared to PTFE (0.5 for O and H, 0.47 for F). Regarding the energy spectra represented in Figure 5, it appears that the spectrum shape is strongly modified by the depth of emission in the filter. For both types of filters, energy spectra for the surface layer are identical, as expected for negligible $\alpha$ attenuation. In marked contrast, energy spectra related to inner layers display a similar general pattern for both types of filters, with spectra peaking at lower energy values for deeper layers and low-energy tails becoming more and more prominent. How-

ever, significantly different behaviors can be observed between the two filter types. Noteworthy, peak positions are located at higher energy in PTFE membranes compared to CA filters. Again, this can be explained by a higher $Z/A$ ratio for CA material, and thus by a higher $\mathrm{d}E/\mathrm{d}x$ (according to Bethe-Bloch formula).

Simulated values for detection efficiencies reach a maximum of 41.5 % for the surface layer in each type of filters (Figure 4). This is in strong agreement with the experimental detection efficiency for PTFE membranes (Table 2), hence suggesting that $\alpha$ emission mainly arises from the surface and/or the very first layers of the filter. Contrastingly, the 32.6 % efficiency determined for CA filters cannot be explained by $\alpha$ emission from the shallowest layers. According to the simulation (Figure 4), such a low efficiency implies that $\alpha$ emission is rooted in deeper layers inside the filter, and a depth of 60 µm can be tentatively proposed. The same conclusion can be drawn from energy spectra. While the sharp PTFE experimental spectrum (Figure 1) is very similar to the simulated spectrum for surface emission (Figure 5), the flatten CA experimental spectrum (Figure 1) suggests the contribution of both surface and deep layers. These observations are coherent with the physical nature of the two studied filters and the associated filtration mechanisms [e.g. 25]: while particles entrapment mostly occurs at the surface for membrane filters (PTFE), a significant part of aerosols is stopped at depth in fibrous filters like CA ones.

## 5. A simple algorithm to determine $\alpha$ attenuation from $\alpha$ spectrum shape

The contrasted energy spectra obtained for both CA and PTFE filters (Figure 1) and the impact of $\alpha$ emission depth on the shape of the energy spectrum (derived from simulations, Figure 5) suggest to take advantage of the spectral information in order to determine the depth profile of $\alpha$ particle emission and, therefore, the global detection efficiency of $\alpha$ emitters ($^{214}$Po in the present case). To do so, we developed a simple algorithm based on the decomposition

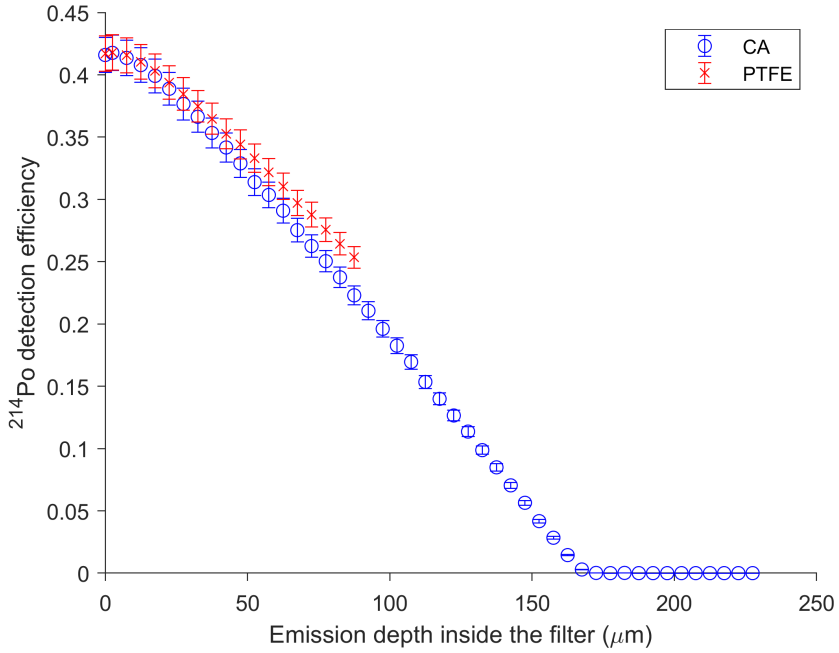


Figure 4: GATE-simulated $^{214}$Po detection efficiency for different depths of emission inside CA and PTFE filters. Each point correspond to a 5 µm-thick layer of emission inside the filters, except for the first point that represents the surface layer. Uncertainties ($2\sigma$) derive from the relative uncertainty of the reference measurement used for the code validation (relative uncertainty of 3.4 %). The detection efficiency values are calculated by integration of the simulated spectrum over the energy region used for experimental efficiency determination (2250 keV to 7500 keV).

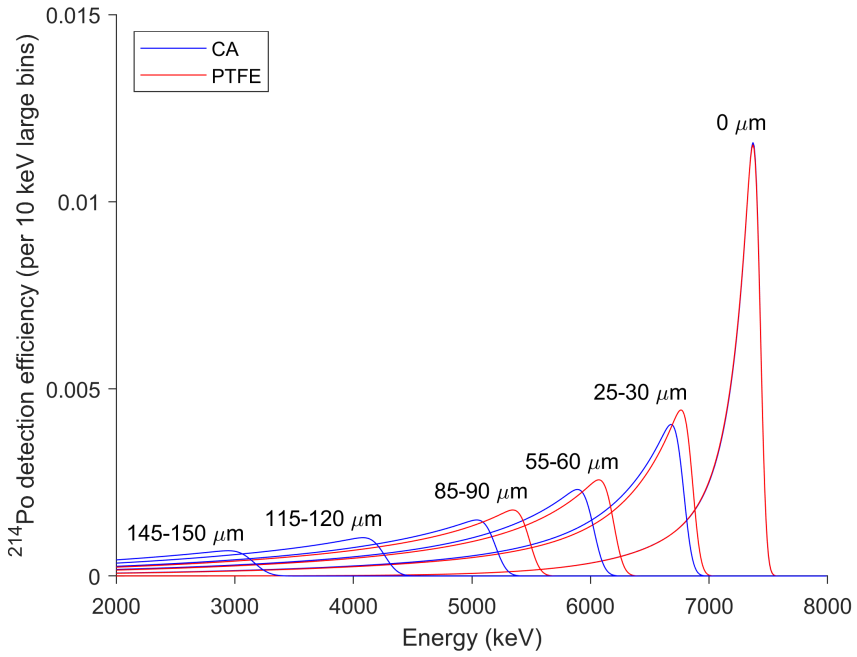


Figure 5: GATE-simulated $^{214}$Po spectra for a few selected depths of emission inside CA and PTFE filters (0 µm, 25 µm to 30 µm, 55 µm to 60 µm, 85 µm to 90 µm, 115 µm to 120 µm and 145 µm to 150 µm). The two last layers are drawn only for CA filters since PTFE filters have a maximum thickness of 90 µm. The depth of emission is indicated on top of the maximum region of each spectrum.

of the experimental energy spectrum on the base of individual-layer simulated energy spectra.

*5.1. Decomposition of the energy spectrum*

Since the contributions of each layer to the global spectrum are independent one from each other, this decomposition is linear and can be written as :

$$\boldsymbol{h}_{\text{obs}} = \boldsymbol{G}\boldsymbol{w} \tag{1}$$

where $\boldsymbol{h}_{\text{obs}}$ refers to the measured global energy spectrum (in counts per energy channel), $\boldsymbol{w}$ refers to the number of $^{214}$Po decays in each layer of the filter and $\boldsymbol{G}$ refers to the simulated efficiencies for each layer and each channel. $\boldsymbol{h}_{\text{obs}}$ and $\boldsymbol{w}$ are vectors of dimension $n_{\text{ch}}$ (number of channels in the experimental spectrum) and $n_{\text{layers}}$ (number of layers simulated in the filter), respectively. $\boldsymbol{G}$ is a matrix of dimension $n_{\text{ch}} \times n_{\text{layers}}$. In our case, $n_{\text{layers}}$ is 19 for PTFE and 35 for CA (the total number of layers is 47 but the last 12 layers have a null detection efficiency, see Figure 4) , and $n_{\text{ch}}$ is 140. Such a linear problem is found to be ill-posed for several reasons. First, this is an overdetermined problem with more equations than unknowns, which implies that an exact mathematical solution may not exist. Such an issue is easily bypassed by searching for a decomposition vector that best reproduces the data $\boldsymbol{h}_{\text{obs}}$, instead of the exact solution. This best solution can be obtained through classical least-square minimization :

$$\boldsymbol{w}_s = (\boldsymbol{G}^T\boldsymbol{C}_d\boldsymbol{G})^{-1}\boldsymbol{G}^T\boldsymbol{C}_d^{-1} \times \boldsymbol{h}_{\text{obs}} \tag{2}$$

where $\boldsymbol{C}_d$ refers to the covariance matrix of the data, $^T$ to the tranpose matrix and $^{-1}$ to the inverse matrix. In the present case, $\boldsymbol{C}_d$ can be assumed diagonal since the binned count numbers are independent random variables. Each diagonal term of $\boldsymbol{C}_d$ is equal to the variance of the count number in the corresponding bin of the spectrum. Moreover, since only one radionuclide is considered here, the number of counts per bin is a Poisson random variable and therefore the diagonal terms of $\boldsymbol{C}_d$ are simply equals to the bin counts :

$$\boldsymbol{C}_d(i) = \boldsymbol{h}_{\text{obs}}(i) \tag{3}$$

Second issue, the problem is also ill-posed because the matrix $\boldsymbol{G}$ is badly conditionned meaning that a small variation in $\boldsymbol{h}_{\text{obs}}$ can induce an important variation of the solution $\boldsymbol{w}_s$ (condition number of $\approx 200$). Contrary to the above-mentioned issue, this feature does not come from the over-determination of the mathematical problem but instead from the important overlapping between the different simulated energy spectra. As a consequence, the inverse problem given by equation 2 might be very sensitive to random fluctuations in $\boldsymbol{h}_{\text{obs}}$ and over-fitting may be observed, resulting in a non-physical solution. In order to address this issue, a Tikhonov regularization was performed following:

$$\boldsymbol{w}_s = (\boldsymbol{G}^T\boldsymbol{C}_d\boldsymbol{G} + \boldsymbol{\Gamma}^T\boldsymbol{\Gamma})^{-1}\boldsymbol{G}^T\boldsymbol{C}_d^{-1} \times \boldsymbol{h}_{\text{obs}} \tag{4}$$

where $\boldsymbol{\Gamma}$ is the Tikhonov regularization matrix. In this work, $\boldsymbol{\Gamma}$ was chosen to be equal to $\lambda\boldsymbol{D}_2$ where $\lambda$ is a real number and $\boldsymbol{D}_2$ is the finite difference operator of order 2 (see Appendix). $\boldsymbol{D}_2$ is such that $\boldsymbol{D}_2\boldsymbol{w}_s$ corresponds to the variations of the depth profile between consecutive layers. This choice is based on the prior knowledge that the solution might be regular and present small finite differences between its components. Depth-distribution of aerosol particles in filters is indeed known to follow a smooth continuum [e.g., 1] and therefore, the depth-profile of $\alpha$ emission from $^{214}$Po should also present a continuous shape. The addition of the regularization matrix in equation 4 forces the solution $\boldsymbol{w}_s$ to be more regular than the solution obtained by the standard approach (equation 4). However, there is no prior knowledge on what should be the value of $\lambda$. This value must be chosen in order to allow a good compromise between the regularity of the solution and the residuals between the original data and the reconstructed spectrum. A low value of $\lambda$ will generate a poorly regular solution with minimal residuals. Contrastingly, a high value of $\lambda$ may give a very regular depth-profile but lead to an important misfit with the experimental data. In order to choose the value of $\lambda$, the L-curve approach was implemented [26]. It simply consists in solving equation 4 for many values of $\lambda$ and plotting a regularity proxy (e.g., the norm of the finite differences of the solution components, $|\boldsymbol{D}_2\boldsymbol{w}_s|$) as a function of the misfit (e.g., the reduced $\chi^2$). The value of $\lambda$ is then taken at the

inflexion point of the L-curve between the high misfit and the poorly-regular end-member solutions. The associated uncertainties can be obtained from the data standard-deviation using the following formula :

$$\boldsymbol{C}_w = \boldsymbol{G}^{-\boldsymbol{g}} \boldsymbol{C}_d (\boldsymbol{G}^{-\boldsymbol{g}})^T \tag{5}$$

where $\boldsymbol{G}^{-\boldsymbol{g}}$ is the generalized inverse of $\boldsymbol{G}$, i.e. $(\boldsymbol{G}^T \boldsymbol{C}_d \boldsymbol{G} + \boldsymbol{\Gamma}^T \boldsymbol{\Gamma})^{-1} \boldsymbol{G}^T \boldsymbol{C}^{-1}$. This estimate only includes the statistical source of uncertainty. The detection efficiency $r$ can be finally calculated using the simulated detection efficiencies :

$$r = \left( \sum_{i=1}^{n_{\text{layers}}} \boldsymbol{w}_s(i) \right)^{-1} \boldsymbol{r}_{\text{simu}}^T \boldsymbol{w}_s \tag{6}$$

where $\boldsymbol{r}_{\text{simu}}$ is a vector representing the simulated detection efficiencies for each layer of the filter. The uncertainty on $r$ can be then calculated using the covariance matrix of the depth-profile $\boldsymbol{C}_w$ :

$$\sigma_r = \left( \sum_{i=1}^{n_{\text{layers}}} \boldsymbol{w}_s(i) \right)^{-1} (\boldsymbol{r}_{\text{simu}}^T \boldsymbol{C}_w \boldsymbol{r}_{\text{simu}})^{1/2} \tag{7}$$

In order to evaluate the effect of $\lambda$ on the detection efficiency, a value of $r$ was calculated for each value of $\lambda$ tested in the L-curve. It was found that the standard deviation is equivalent to the uncertainty determined from equation 7, i.e. of the order of a few 0.1 % of detection efficiency.

### *5.2. Validation of the algorithm*

This method was applied to both CA and PTFE filters taken in the underground cellar in Clermont-Ferrand. Results are reported in Table 3 and plotted in Figures 6 and 7. Figure 6 compares the reconstructed energy spectra with the measured spectra for both filters. It can be observed that a good agreement is obtained in both cases, with residuals typically lower than 10 %. Exceptions include the low-energy region of PTFE spectrum and the right-sided tail of CA spectrum, for which residuals may reach up to 20 %. This suggests that some processes are incorrectly described in the simulation, such as the extent of the low energy tail or else the detector energy resolution). However, these outliers represent only a small fraction of the total number of counts and are unlikely to

(a)

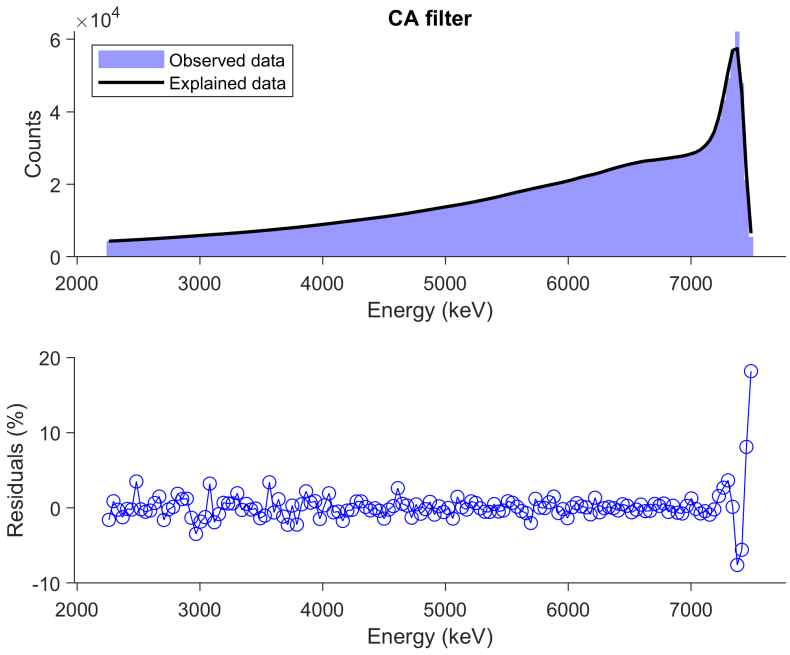


(b)

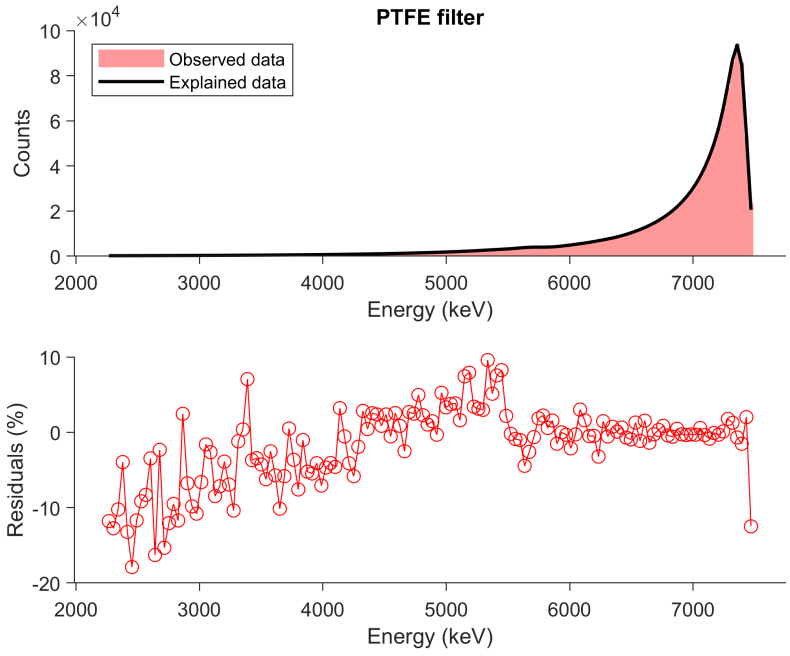


Figure 6: Comparison of experimental and reconstructed $\alpha$ spectra for (a) CA and (b) PTFE filters.

Table 3: Comparison of $^{214}$Po detection efficiency for CA and PTFE filters determined from $^{214}$Bi $\gamma$ measurement or from $\alpha$ spectrum inversion. The $2\sigma$uncertainties are derived from both counting statistics and the fit procedure for the $^{214}$Bi-based determination, and from the overall 3.4 % uncertainty on the reference source activity for the $\alpha$ spectrum inversion. Note that this latter value is much more important than the uncertainty given by equation 7 (typically 0.5 %, relative).

| $^{214}$Po detection efficiency | CA | PTFE |
|---|---|---|
| by $\gamma$ measurement of $^{214}$Bi | 32.6(3) % | 39.8(6) % |
| by $\alpha$ spectrum inversion | 31.4(11) % | 41.0(14) % |

bias the detection efficiency determined from the inversion of the spectrum. As a matter of fact, the inferred efficiencies are undistinguishable, within uncertainties, from the reference values obtained from $^{214}$Bi $\gamma$ spectrometry (see Table 3), which validates our methodology. Therefore, it can be applied to determine $\alpha$ attenuation from the shape of an energy spectrum without prior knowledge of the depth of entrapment of aerosol particles, thus allowing easy and accurate determination of $\alpha$ emitter activities collected on the surface of and trapped in aerosol filters

### *5.3. Limitations*

While the $^{214}$Po detection efficiency can be accurately determined from the shape-analysis of the $\alpha$ energy spectrum, the inferred depth-profiles of $\alpha$ emission may not be fully representative of the actual repartition of $^{214}$Po atoms in the filter. The inversion process is indeed very unstable and according to the value of the regularization parameter $\lambda$, the resulting profile can significantly vary. Therefore, dedicated tests should be performed in order to validate the spectrum inversion method for the specific determination of depth-profiles, for instance using pealing techniques [9]. Yet, the inferred depth-profiles for CA and PTFE filters (see Figure 7) correspond well to the expected profiles for each type of filters. $\alpha$ emitters indeed appear mostly concentrated at the surface of the PTFE membrane (more than 80 % within the first 5 µm) while

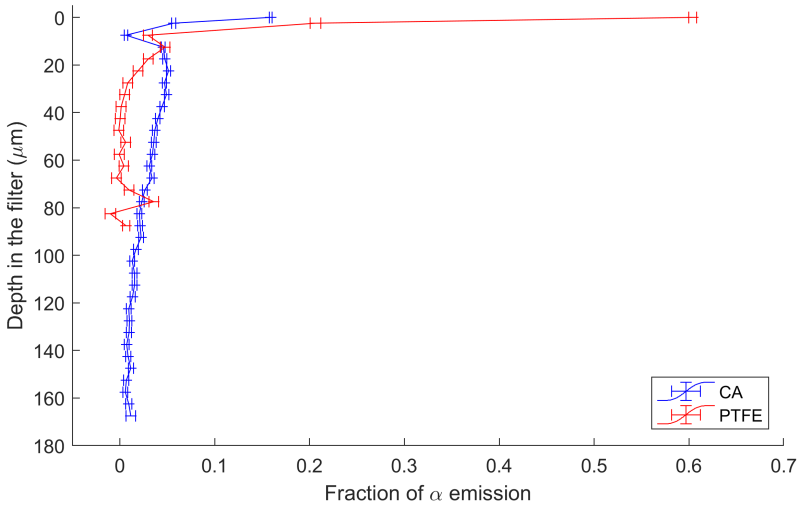


Figure 7: Depth-profiles of $\alpha$ emission in CA and PTFE filters. Uncertainties ($2\sigma$) are computed from equation 5.

they are spread throughout the CA filter thickness (less than 30 % of $\alpha$ emitters within the first 5 µm). Furthermore, it is worth noting that although the quantity of $^{214}$Po determined for each layer may vary according to the value of $\lambda$, the overall detection efficiency does not depend much on the regularization parameter (maximal variations in detection efficiency ($\pm 0.1$ %) within the $\lambda$ range $10^{-5}$ a to $10^{-3}$ are of the same order as the uncertainty derived from statistical fluctuations of experimental counts). This suggests that the proposed method could be applied even without giving an important weight to the regularization process.

Our results also show that the $\alpha$ attenuation difference between CA and PTFE filters is not due to a difference in the attenuating power of the two materials. Both materials are indeed of rather similar compositions in terms of both $Z/A$ ratio and density. Accordingly, for a given layer, that is for the same depth of emission within the filter, the simulation predicts rather similar detection efficiencies (see Figure 4). The marked different behavior between the two types is instead best explained by the distribution of $\alpha$ emitters within the

filter. In the case of the CA filter, aerosol particles likely penetrate at important depths ($> 20\,\mu m$) while they would mostly remain in the first $5\,\mu m$ for PTFE membranes. Morevover, numerical simulation predicts a total attenuation of $^{214}$Po $\alpha$ particles after $180\,\mu m$. If $^{214}$Po atoms were also accumulated in the filter at these depths, it would thus be impossible to infer their presence from the $\alpha$ spectrum shape. Consequently, our method is blind after $180\,\mu m$ and our result for CA filter must be regarded as a maximum estimate of the detection efficiency. Meanwhile, $\gamma$ measurement of $^{214}$Bi is not affected by the emission position in the filter and the attenuation estimated from this measurement also includes the potential atoms trapped below $180\,\mu m$. Yet, even if the $\gamma$-based estimation is higher than the $\alpha$-based estimation, both values are not significantly different within uncertainties. Although it cannot be ruled out that some $^{214}$Po atoms are also trapped deeper than $180\,\mu m$ beneath the filter surface, these deeply trapped atoms would then represent a minor fraction and would bias our estimate by less than a few %.

## 6. Conclusion

The $\alpha$ attenuation within cellulose acetate and PTFE air filters used for radiological monitoring and volcanology has been assessed by simultaneous $\alpha$ and $\gamma$ spectrometry of the $^{214}$Bi-$^{214}$Po pair. The detection efficiency of $^{214}$Po is found to be significantly lower for cellulose acetate filters compared to PTFE filters, with a difference of 10 % yield. In addition, while the $^{214}$Po $\alpha$ spectrum defines a sharp peak on PTFE membranes, it presents a much more pronounced low-energy tail for CA filters as a consequence of enhanced $\alpha$ attenuation. Monte Carlo simulations of $\alpha$ particles interaction within the filters suggest that this difference is related to a deeper entrapment of aerosol particles inside cellulose acetate matrices.

We therefore developed a method to infer $\alpha$ attenuation from the sole shape of the $\alpha$ energy spectrum. This method relies on the decomposition of the

measured $\alpha$ spectrum as a linear combination of simulated spectra corresponding to variable depths of $\alpha$ particle emission. It generates a depth distribution which can in turn be used to compute $\alpha$ attenuation. The inferences obtained from this method compare very well with experimental values of detection effiencies and demonstrate that this method can be used to correct for $\alpha$ attenuation in air filters. This work also suggests that previously published estimates of the long-lived $^{210}$Po emissions of volcanic origin likely are underestimated (because of $\alpha$ attenuation with both cellulose acetate fibers and volcanic ash accumulated on the filter surface) and should be revised using the method proposed in this paper.

Provided that new simulations are run, the method presented in this paper could also apply to many other types of filters, including glass fiber or polycarbonate filters, and a variety of $\alpha$ emitters, including articial and natural radionuclides. In this study, the achieved precision is of the order of 5 % ($2\sigma$). It is currently limited by the uncertainties of reference measurements used for validation (either for the simulation design or for the inversion process) and it could be easily improved using radioactive sources with a better-determined activity.

**Acknowledgements**

We thank Gérard Pioche for granting access to his underground cellar and Lydia Maigne (LPC) for her advice on the simulation part of this work, especially on the use of the GATE code. We also thank Hélène Fonvieille and Alain Falvard (LPC) for helpful discussions in the course of this study. Part of this research was undertaken in the framework of the EC Project EuroVolc (WP5 and WP10). This is ClerVolc contribution N°XXX.

## Appendix A.

The finite difference operator of order 2 (matrix $\boldsymbol{D}_2$ of dimension $(n_{\text{layers}} - 1) \times n_{\text{layers}}$) introduced in section 5.1 is defined as follows:

$$\boldsymbol{D}_2 = \begin{pmatrix} 1 & -1 & & 0 \\ & \ddots & \ddots & \\ 0 & & 1 & -1 \end{pmatrix} \tag{A.1}$$

## References


[1] D. P. Higby, Effects of particle size and velocity on burial depth of airborne particles in glass fiber filters, Tech. Rep. PNL–5278, Pacific Northwest Lab. (1984).
URL http://inis.iaea.org/Search/search.aspx?orig_q=RN:16053627

[2] M. E. Moore, A. R. McFarland, J. C. Rodgers, Factors That Affect Alpha Particle Detection in Continuous Air Monitor Applications, Health Physics 65 (1) (1993) 69–81.
URL https://journals.lww.com/health-physics/Abstract/1993/07000/Factors_That_Affect_Alpha_Particle_Detection_in.8.aspx

[3] S. Pickering, The interpretation of alpha energy spectra from particulate sources, Journal of Aerosol Science 15 (5) (1984) 533–543. doi:10.1016/0021-8502(84)90016-8.
URL http://www.sciencedirect.com/science/article/pii/0021850284900168

[4] S. Huang, S. D. Schery, R. E. Alcantara, J. C. Rodgers, P. T. Wasiolek, Influence of dust loading on the alpha-particle energy resolution of continous air monitors for thin deposits of radioactive aerosols, Health Physics 83 (6) (2002) 884–891.
URL https://journals.lww.com/health-physics/Abstract/2002/12000/INFLUENCE_OF_DUST_LOADING_ON_THE_ALPHA_PARTICLE.16.aspx

[5] J. W. Luetzelschwab, C. Storey, K. Zraly, D. Dussinger, Self absorption of alpha and beta particles in a fiberglass filter, Health Physics 79 (4) (2000) 425–430.
URL https://journals.lww.com/health-physics/Abstract/2000/10000/Self_Absorption_of_Alpha_and_Beta_Particles_in_A.12.aspx

[6] T. Geryes, C. Monsanglant-Louvet, Determination of correction factors for alpha activity measurements in the environment (conditions of high dust loading), Radiation Protection Dosimetry 144 (1-4) (2011) 659–662, publisher: Oxford Academic. doi:10.1093/rpd/ncq451.
URL https://academic.oup.com/rpd/article/144/1-4/659/1616925

[7] T. Geryes, C. Monsanglant-Louvet, E. Gehin, Effects of filtration velocity on the measurements of radioactive aerosols in filters, in: Proceeding of the European Aerosol Conference, 2008, pp. 24–29.

[8] T. Siiskonen, R. Pöllänen, Simulation of alpha particle spectra from aerosol samples, Applied Radiation and Isotopes 60 (6) (2004) 947–953. doi:10.1016/j.apradiso.2004.02.021.
URL http://www.sciencedirect.com/science/article/pii/S0969804304000685

[9] T. Geryes, C. Monsanglant-Louvet, L. Berger, E. Gehin, Application of the monte carlo method to study the alpha particle energy spectra for radioactive aerosol sampled by an air filter, Health Physics 97 (2) (2009) 125–131. doi:10.1097/01.HP.0000348000.29119.e7.
URL https://journals.lww.com/health-physics/Abstract/2009/08000/APPLICATION_OF_THE_MONTE_CARLO_METHOD_TO_STUDY_THE.4.aspx

[10] T. Geryes, Etude expérimentale et numérique de la dégradation de la mesure nucléaire d'aérosols radioactifs prélevés avec desfiltres de surveillance, PhD Thesis, Université Paris-Est (2011).

[11] T. Siiskonen, R. Pöllänen, New approach to alpha spectrum analysis. Iterative Monte Carlo simulations and fitting, Progress in Nuclear Science and Technology 2 (2011) 437–441. doi:10.15669/pnst.2.437.
URL http://inis.iaea.org/Search/search.aspx?orig_q=RN:49052083

[12] P.-J. Gauthier, O. Sigmarsson, M. Gouhier, B. Haddadi, S. Moune, Elevated gas flux and trace metal degassing from the 2014–2015 fissure eruption at the Bárðarbunga volcanic system, Iceland, Journal of Geophysical Research: Solid Earth 121 (3) (2016) 1610–1630. doi:10.1002/2015JB012111.
URL https://agupubs.onlinelibrary.wiley.com/doi/abs/10.1002/2015JB012111

[13] L. Terray, P.-J. Gauthier, V. Breton, S. Giammanco, O. Sigmarsson, G. Salerno, T. Caltabiano, A. Falvard, Radon Activity in Volcanic Gases of Mt. Etna by Passive Dosimetry, Journal of Geophysical Research: Solid Earth 125 (9), number: 9 _eprint: https://agupubs.onlinelibrary.wiley.com/doi/pdf/10.1029/2019JB019149. doi:10.1029/2019JB019149.
URL https://agupubs.onlinelibrary.wiley.com/doi/abs/10.1029/2019JB019149

[14] C. Monsanglant-Louvet, M. Osmond, L. Ferreux, N. Liatimi, A. Maulard, J. L. Picolo, B. Marcillaud, F. Gensdarmes, Production of reference sources of radioactive aerosols in filters for proficiency testing, Applied Radiation and Isotopes 95 (2015) 13–22. doi:10.1016/j.apradiso.2014.09.014.
URL http://www.sciencedirect.com/science/article/pii/S0969804314003376

[15] G. Polian, G. Lambert, Radon daughters and sulfur output from Erebus volcano, Antarctica, Journal of Volcanology and Geothermal Research 6 (1) (1979) 125–137. doi:10.1016/0377-0273(79)90050-7.

URL http://www.sciencedirect.com/science/article/pii/0377027379900507

[16] M. Le Cloarec, M. Pennisi, Radionuclides and sulfur content in Mount Etna plume in 1983–1995: new constraints on the magma feeding system, Journal of Volcanology and Geothermal Research 108 (1-4) (2001) 141–155. doi:10.1016/S0377-0273(00)00282-1.
URL https://linkinghub.elsevier.com/retrieve/pii/S0377027300002821

[17] A. G. Allen, P. J. Baxter, C. J. Ottley, Gas and particle emissions from Soufrière Hills Volcano, Montserrat, West Indies: characterization and health hazard assessment, Bulletin of Volcanology 62 (1) (2000) 8–19. doi:10.1007/s004450050287.
URL https://doi.org/10.1007/s004450050287

[18] C. Rizo-Maestre, V. Echarri-Iribarren, Radon Gas in the City of Alicante. High Risk of Low Indoor Air Quality in Poorly Ventilated Buildings, International Journal of Environmental Research and Public Health 17 (23) (2020) 8762, number: 23 Publisher: Multidisciplinary Digital Publishing Institute. doi:10.3390/ijerph17238762.
URL https://www.mdpi.com/1660-4601/17/23/8762

[19] S. Jan, G. Santin, D. Strul, S. Staelens, K. Assié, D. Autret, S. Avner, R. Barbier, M. Bardiès, P. M. Bloomfield, D. Brasse, V. Breton, P. Bruyndonckx, I. Buvat, A. F. Chatziioannou, Y. Choi, Y. H. Chung, C. Comtat, D. Donnarieix, L. Ferrer, S. J. Glick, C. J. Groiselle, D. Guez, P.-F. Honore, S. Kerhoas-Cavata, A. S. Kirov, V. Kohli, M. Koole, M. Krieguer, D. J. v. d. Laan, F. Lamare, G. Largeron, C. Lartizien, D. Lazaro, M. C. Maas, L. Maigne, F. Mayet, F. Melot, C. Merheb, E. Pennacchio, J. Perez, U. Pietrzyk, F. R. Rannou, M. Rey, D. R. Schaart, C. R. Schmidtlein, L. Simon, T. Y. Song, J.-M. Vieira, D. Visvikis, R. V. d. Walle, E. Wieërs, C. Morel, GATE: a simulation toolkit for PET and SPECT, Physics in

Medicine and Biology 49 (19) (2004) 4543–4561, publisher: IOP Publishing. doi:10.1088/0031-9155/49/19/007.
URL https://doi.org/10.1088%2F0031-9155%2F49%2F19%2F007

[20] S. Agostinelli, J. Allison, K. Amako, J. Apostolakis, H. Araujo, P. Arce, M. Asai, D. Axen, S. Banerjee, G. Barrand, F. Behner, L. Bellagamba, J. Boudreau, L. Broglia, A. Brunengo, H. Burkhardt, S. Chauvie, J. Chuma, R. Chytracek, G. Cooperman, G. Cosmo, P. Degtyarenko, A. Dell'Acqua, G. Depaola, D. Dietrich, R. Enami, A. Feliciello, C. Ferguson, H. Fesefeldt, G. Folger, F. Foppiano, A. Forti, S. Garelli, S. Giani, R. Giannitrapani, D. Gibin, J. J. Gómez Cadenas, I. González, G. Gracia Abril, G. Greeniaus, W. Greiner, V. Grichine, A. Grossheim, S. Guatelli, P. Gumplinger, R. Hamatsu, K. Hashimoto, H. Hasui, A. Heikkinen, A. Howard, V. Ivanchenko, A. Johnson, F. W. Jones, J. Kallenbach, N. Kanaya, M. Kawabata, Y. Kawabata, M. Kawaguti, S. Kelner, P. Kent, A. Kimura, T. Kodama, R. Kokoulin, M. Kossov, H. Kurashige, E. Lamanna, T. Lampén, V. Lara, V. Lefebure, F. Lei, M. Liendl, W. Lockman, F. Longo, S. Magni, M. Maire, E. Medernach, K. Minamimoto, P. Mora de Freitas, Y. Morita, K. Murakami, M. Nagamatu, R. Nartallo, P. Nieminen, T. Nishimura, K. Ohtsubo, M. Okamura, S. O'Neale, Y. Oohata, K. Paech, J. Perl, A. Pfeiffer, M. G. Pia, F. Ranjard, A. Rybin, S. Sadilov, E. Di Salvo, G. Santin, T. Sasaki, N. Savvas, Y. Sawada, S. Scherer, S. Sei, V. Sirotenko, D. Smith, N. Starkov, H. Stoecker, J. Sulkimo, M. Takahata, S. Tanaka, E. Tcherniaev, E. Safai Tehrani, M. Tropeano, P. Truscott, H. Uno, L. Urban, P. Urban, M. Verderi, A. Walkden, W. Wander, H. Weber, J. P. Wellisch, T. Wenaus, D. C. Williams, D. Wright, T. Yamada, H. Yoshida, D. Zschiesche, Geant4—a simulation toolkit, Nuclear Instruments and Methods in Physics Research Section A: Accelerators, Spectrometers, Detectors and Associated Equipment 506 (3) (2003) 250–303. doi:10.1016/S0168-9002(03)01368-8.

URL https://www.sciencedirect.com/science/article/pii/S0168900203013688

[21] A. Smith, P. Wynn, P. Barker, Natural and anthropogenic factors which influence aerosol distribution in Ingleborough Show Cave, UK, International Journal of Speleology 42 (1). doi: http://dx.doi.org/10.5038/1827-806X.42.1.6 .
URL https://digitalcommons.usf.edu/ijs/vol42/iss1/6

[22] J. Dredge, I. J. Fairchild, R. M. Harrison, A. Fernandez-Cortes, S. Sanchez-Moral, V. Jurado, J. Gunn, A. Smith, C. Spötl, D. Mattey, P. M. Wynn, N. Grassineau, Cave aerosols: distribution and contribution to speleothem geochemistry, Quaternary Science Reviews 63 (2013) 23–41. doi:10.1016/j.quascirev.2012.11.016.
URL https://linkinghub.elsevier.com/retrieve/pii/S0277379112004878

[23] G. Steinhoff, O. Haupt, W. Dannecker, Fast determination of trace elements on aerosol-loaded filters by X-ray fluorescence analysis considering the inhomogeneous elemental distribution, Fresenius' Journal of Analytical Chemistry 366 (2) (2000) 174–177. doi:10.1007/s002160050034.
URL https://doi.org/10.1007/s002160050034

[24] R. Casanovas, J. J. Morant, M. Salvadó, Energy and resolution calibration of NaI(Tl) and LaBr3(Ce) scintillators and validation of an EGS5 Monte Carlo user code for efficiency calculations, Nuclear Instruments and Methods in Physics Research Section A: Accelerators, Spectrometers, Detectors and Associated Equipment 675 (2012) 78–83. doi:10.1016/j.nima.2012.02.006.
URL http://www.sciencedirect.com/science/article/pii/S0168900212001490

[25] A. Renoux, D. Boulaud, Les aérosols: physique et métrologie, Tec & Doc Lavoisier, 1998.

[26] C. L. Lawson, R. J. Hanson, Solving least squares problems, SIAM, 1995.